Near- and Far-Field Observation of Phonon Polaritons in Wafer Scale Multilayer Hexagonal Boron Nitride Prepared by Chemical Vapor Deposition

Eugenio Calandrini, Kirill Voronin, Osman Balci, Maria Barra Burillo, Andrei Bylinkin, Sachin M. Shinde, Subash Sharma, Felix Casanova, Luis E. Hueso, Andrei Chuvilin, Clifford McAleese, Ben R. Conran, Xiaochen Wang, Teo Kenneth, Valentyn S. Volkov, Andrea C. Ferrari, Alexey Y. Nikitin, and Rainer Hillenbrand*

E. Calandrini, M. Barra Burillo, A. Bylinkin, F. Casanova, L. Hueso, A. Chuvilin, R. Hillenbrand

CIC nanoGUNE BRTA, Tolosa Hiribidea, 76, 20018, Donostia - San Sebastián, Spain

Email: r.hillenbrand@nanogune.eu.

K. Voronin, A. Bylinkin, A.Y. Nikitin

Donostia International Physics Center (DIPC), Paseo Manuel de Lardizabal, 4, 20018 Donostia - San Sebastián, Spain

O. Balci, S.M. Shinde, S. Sharma, A. C. Ferrari

Cambridge Graphene Centre, University of Cambridge, 9 JJ Thomson Ave, Cambridge CB3 0FA, United Kingdom

F. Casanova, L. E. Hueso, A. Chuvilin, A.Y. Nikitin, R. Hillenbrand

IKERBASQUE, Basque Foundation for Science, Bilbao, Spain

C. McAleese, B. R. Conran, X. Wang, K.B.K Teo

AIXTRON Ltd. Buckingway Business Park, Anderson Rd, Swavesey, Cambridge CB244FQ, UK

V. S. Volkov

XPANCEO, Bayan Business Center, DIP, 607-0406, Dubai, UAE

Abstract

Polaritons in layered materials (LMs) are a promising platform to manipulate and control light at the nanometer scale. Thus, the observation of polaritons in wafer-scale LMs is critically important for the development of industrially relevant nanophotonics and optoelectronics applications. Here we report phonon polaritons (PhPs) in wafer-scale multilayer hexagonal boron nitride (hBN) grown by chemical vapor deposition. By infrared nanoimaging we visualize the PhPs and measure their lifetime of about 0.6 ps, comparable to that of micromechanically exfoliated multilayer hBN. We also demonstrate PhP nano-resonators with quality factors of about 50, which is 0.7 times that of state of-the-art devices based on exfoliated hBN. Our results could enable PhP-based surface-enhanced infrared spectroscopy (e.g. for gas sensing) and infrared photodetector applications.

1. Introduction

Polaritons are electromagnetic (EM) waves formed by coupling of light to dipolar material excitations such as plasmons, phonons or excitons. They are at the centre of an ever-growing research effort due to the possibility to confine and manipulate light at the nanometer scale. Recently, layered materials (LMs) have opened new avenues for polariton-based nanophotonics.[1,2] Plasmon and phonon polaritons, for example in graphene[3] and polar materials such as hBN,[4] α-MoO$_3$[5] and α-V$_2$O$_5$,[6] respectively, can propagate with unpreceded short wavelengths and field confinement, long lifetimes and anomalous wavefronts.[1,2,7] They promise manifold future applications, such as ultra-sensitive surface-enhanced infrared spectroscopy (SEIRA) based on polariton resonators,[8–11] deep subwavelength-scale infrared waveguiding[12,13] and ultrafast nanoscale heat transfer.[14,15]

Most LM polariton experiments and applications so far rely on the micromechanical exfoliation of individual flakes from their bulk crystals, which is not sufficient for an efficient and scalable fabrication of polariton-based sensors and devices. Synthesis of millimeter-scale layers of LM materials will be thus of critical importance, since they will offer the advantages of, for example, (i) fabricating large-scale polariton nanoresonator arrays to improve the signal-to-noise ratio and thus the sensitivity in SEIRA applications, (ii) superior control of layer thicknesses and their homogeneity, and (iii) scalable and reproducible fabrication of large amounts of structures and devices, which will be a prerequisite for implementing LM polaritonics into future real-world applications. Large-scale graphene layers can be
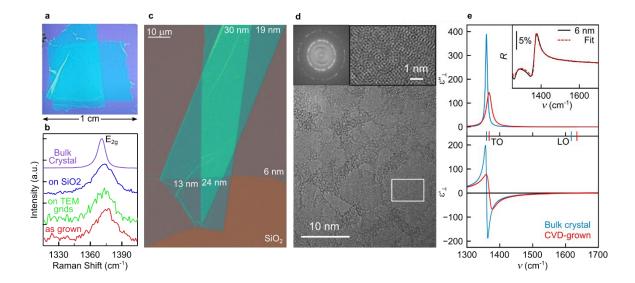
2

already grown in good quality by chemical vapor deposition (CVD)[16] and plasmonic applications such as SEIRA[8,17,18] and plasmon-assisted infrared photodetection[19] have been already demonstrated. The large-scale growth of other LM materials, however, is still in its infancy, particularly that of polar LM materials hosting phonon polaritons (PhPs) that outperform graphene plasmons because of their much larger lifetimes (up to 8 ps[5]). Only recently, high-quality PhP resonators based on bottom-up synthesis were demonstrated with chemically synthesized MoO_3 ribbons of 120 nm thickness[20] and PhPs propagation was reported on millimeter-scale free-standing SiC membranes.[21] However, large-scale films of LM materials of several nm thickness have not been reported so far but are needed for integration of LM-based PhP devices into CMOS compatible fab-process lines.

CVD-growth of high-quality, large-scale polar LMs has been reported,[22–24] however, PhPs have been observed only in CVD grown mono-, bi-, and tri-layers hBN,[25] where the PhP wavelength is extremely short (in the range of few nanometers) and thus challenges the development of PhP-based resonators and devices. For that reason, the growth of large-scale multilayer hBN (ML-hBN) with thicknesses of several nanometers is critically important to allow for the fabrication of larger resonator structures to relax fabrication constraints and to increase the coupling efficiency between light and LM phonon polariton resonators (as the scattering cross sections scale with the resonator volume).

Here we report wafer-scale ML-hBN, up to 24 nm thick, supporting PhPs with lifetimes of about 0.6 ps. We verify the PhPs via polariton interferometry with a scattering-type scanning near-field optical microscopy (s-SNOM). Random PhP interference patterns are observed, which we explain by PhP scattering at randomly distributed defects. By analysis of these patterns we measure the PhP dispersion, propagation lengths and lifetimes. All of them agree well with calculations based on the dielectric function of the ML-hBN, which was obtained from far-field infrared reflection spectroscopy. Our results show that PhP scattering at the defects does not have a significant influence on the PhP dispersion and damping. Consequently, Fabry-Perot PhP nanoresonators, that we fabricated from ML-hBN, exhibit remarkable quality factors of about $Q \approx 50$, approaching that of PhP nanoresonators made of micromechanically exfoliated hBN (ME-hBN).

3

Figure 1. Structural and optical characterization of ML-hBN. a) Photograph of two cm-scale hBN multilayers transferred onto a 1×1 cm^2 SiO$_2$/Si substrate. b) Raman spectra of as grown and transferred CVD ML-hBN (acquired with 514.5 nm laser wavelength) and ME-hBN as reference.[26,27] c) Light microscope image of a 6 nm thick layer that was folded during the transfer onto a Si/SiO$_2$ substrate. Numbers indicate the respective total layer thickness (measured by AFM). d) Transmission Electron Microscopy image of 1 nm-thick ML-hBN. Top right inset: enlarged view of the area marked by the small white square in the center of the image. Top left inset: FT of the image. e) Red curves show the real (bottom) and imaginary (top) part of the infrared in-plane component of dielectric tensor of the ML-hBN, obtained by fitting the infrared reflection spectrum (inset) of a 6 nm-thick multilayer. For comparison, the blue curves show that one of hBN crystals.[28]

2. Results

The large-scale ML-hBN was grown on a sapphire substrate in an AIXTRON CCS 2D reactor (https://www.aixtron.com/en) as described in Methods section. **Figure 1a** shows a photograph of two ML-hBN layers that were transferred onto a SiO$_2$/Si substrate (see Methods), demonstrating that centimeter-scale layers can be obtained and stacked uniformly. The thickness and roughness (RMS) of the transferred ML-hBN are about 5.5 and 0.9 nm, respectively, as measured form atomic force microscopy (AFM) images such as the ones shown in Figure 2b. A closer inspection with a light microscope (Figure 1c) of a similar sample reveals that the ML-hBN layers can be folded multiple times, showing that the preparation of several 10 nm-thick layers can be achieved by stacking individual hBN multilayers.

Figure 1b shows Raman spectra of ML-hBN. For the as-grown material on the sapphire substrate we observe a peak at 1371 cm^{-1} (red curve) that shifts to 1368 cm^{-1} after the transfer of ML-hBN onto either the Si/SiO$_2$ substrate or the TEM grid (blue and green curves, respectively), indicating the relaxation of

4

strain generated during the growth process. This peak is blue-shifted by only 2 cm^{-1} with respect to the E$_{2g}$ Raman mode of hBN bulk crystals (purple curve),[26,27] confirming that the growth process yields hBN. On the other hand, the peak linewidth of about 20 cm^{-1} is twice larger than that of bulk hBN, which we attribute to structural imperfections and polycrystallinity found by transmission electron microscopy (TEM). We observe domains, which exhibit moiré-like superlattices with different crystal orientations due to the stacking of polycrystalline 1L-hBN (Figure 1d). Fast Fourier transform (FFT) of the TEM image (top left inset in Figure 1d) shows rings confirming that our ML-hBN is polycrystalline (see Supplementary Information). The top right inset in Figure 1d is the enlarged view of the white square in Figure 1e and shows the moiré-like super lattice in an individual domain. The dark boundaries are due to irregular stacking of 1L-hBN on each other, also indicating polycrystallinity. From the size of the moiré-like domains in Figure 1d we estimate a grain size in the range of 2 to 15 nm.

For measuring the in-plane component of the ML-hBN dielectric tensor, $\varepsilon_\perp(\nu)$, we performed far-field infrared reflection spectroscopy of a 6 nm thick ML-hBN on a SiO$_2$/Si substrate (see Methods). Fitting the reflection spectrum (inset of Figure 1e) by the Fresnel reflection coefficient describing the ML-hBN/SiO$_2$/Si stack (see Methods), we extracted the real and imaginary parts of $\varepsilon_\perp(\nu)$, $\varepsilon_\perp'(\nu)$ and $\varepsilon_\perp''(\nu)$, which are shown in Figure 1e (red curves). For comparison, we show the in-plane component of the dielectric tensor of a layer that was exfoliated from a crystal of naturally abundant hBN (blue curves).[28] Such a comparison is justified because (i) the dielectric function of thin hBN layers is the same as that of bulk hBN crystals, even in the few monolayer limit[29], and (ii) the bulk dielectric function of hBN is typically used to quantitatively describe the dispersion of PhPs in thin exfoliated hBN layers[4,28]. For the CVD-grown layer, we find transversal optical (TO) and longitudinal optical (LO) phonon frequencies at 1369 and 1621 cm^{-1}, respectively, which are blue-shifted by about 8 cm^{-1} compared to that of ME-hBN, corroborating that the CVD-grown layer is hBN. On the other hand, the damping (according to $\varepsilon_\perp''(\nu)$) is a factor of about two larger for the ML-hBN (consistent with the Raman spectroscopy results of Figure 1b), which we attribute to the nanocrystalline structure of the layer and growth defects.

The negative real part of $\varepsilon_\perp(\nu)$ between the TO and LO frequencies promises that this material can support PhPs. We explore this possibility by polariton interferometric nanoimaging of single and stacked ML-hBNs with a scattering-type scanning near-field optical microscope (s-SNOM).[30] As illustrated in **Figure 2a**, the metallized tip of an atomic force microscope (AFM) is illuminated by a p-polarized infrared laser beam. The tip acts as an infrared nanoantenna that concentrates the incident field at its sharp apex, yielding a nanoscale near-field spot for launching the polaritons. The tip-launched polaritons propagate away from the tip and are typically reflected at layer edges and defects. Pseudo-heterodyne interferometric recording the tip-scattered field as a function of tip position (x,y) subsequently yields amplitude and phase images, $s_3(x,y)$ and $\varphi_3(x,y)$, which exhibit polariton interference fringes with a spacing of half the polariton wavelength, $\lambda_p/2$ (see Methods).[4,31,32]
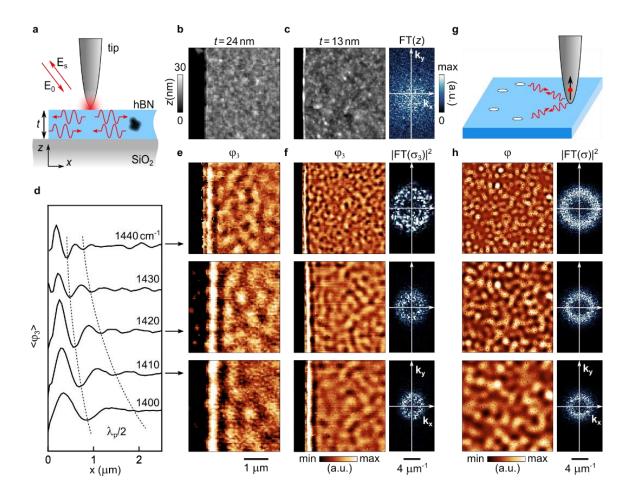
5

Figure 2. Phonon polariton interferometry of ML-hBN. a) Schematics of the experiment. E_0 and E_s denote the electric field of the incident and tip-scattered radiation. b-c) Topography images of the 24 and 13 nm thick ML-hBN. The right image in panel c shows the FT of the topography image of the 13 nm thick ML-hBN. d) Averaged near-field phase line profiles extracted perpendicular to the edge of the phase images shown in panel e. $x = 0$ μm corresponds to the ML-hBN edge. Dashed lines are a guide to the eye, tracing adjacent signal minima. e,f) Near-field phase images $\varphi_3(x, y)$ of the 24 and 13 nm ML-hBN recorded at 1440, 1420 and 1410 cm^{-1} (top to bottom). Right images of panel f: FT of the complex-valued near-field images, $|\hat{\sigma}_3(k_x, k_y)|^2$. g) Schematics of the dipole model for simulating s-SNOM images. A point dipole source (black arrow) and randomly distributed holes (white dots) mimic the AFM tip and the defects in ML-hBN. h) Simulated phase images $\varphi(x, y)$ and FTs of the corresponding complex-valued s-SNOM images, $|\hat{\sigma}(k_x, k_y)|^2$.

Figure 2b and c show the topography images of a 24 nm and a 13 nm thick samples (4 and 2 stacked ML-hBNs, respectively), revealing homogeneous layers with a roughness of about 2.7 nm (RMS). In the infrared s-SNOM phase images φ_3 of the same areas we observe strong signal fluctuations for all

6

the investigated layers. This contrasts with infrared s-SNOM images of ME-hBN, where the interior of the flakes appears homogeneous and PhP interference fringes are observed only close to the edges and parallel to them.[25,32] Interestingly, the periodicity of the signal fluctuations increases with decreasing wavenumber, ν, and with increasing layer thickness, which lets us assume that the infrared s-SNOM pattern is the consequence of PhP interference caused by scattering of PhPs at randomly distributed defects all over the ML-hBN. Our interpretation is supported by the appearance of fringes parallel to the edge of the ML-hBN, whose fringe spacing exhibits the same behavior. From the line profiles shown in Figure 2d (extracted from the infrared images of the 24 nm thick ML-hBN perpendicular to the edge and averaged over 128 lines) we can directly measure the PhP wavelengths, as one signal oscillation period corresponds to $\lambda_p/2$. Measurements for different ν yield the PhP dispersion (black crosses in Figure 3b), which matches well the polariton dispersion that was calculated for a 24 nm thick layer on a SiO$_2$/Si substrate with a dielectric function (red curves in Figure 1e) corresponding to that of the CVD ML-hBN (see Methods).

For the ML-hBNs thinner than 24 nm we barely observe interference fringes parallel to the edge. Further, since they are strongly distorted by random PhP interference patterns. This prevents the direct measurement of the PhP wavelength from the spacing of the fringes parallel to the ML-hBN edges. We thus analyze the random interference pattern (yielding the same PhP properties as the analysis of fringes parallel to the ML-hBN edges, as verified in Figure 3b) via Fourier transform (FT) of the s-SNOM images. Because of the short PhP propagation lengths, it is critically important to perform a complex-valued FT of the complex-valued s-SNOM images, $\sigma_3(x,y) = s_3(x,y)e^{i\varphi_3(x,y)}$, rather than FT of phase $\varphi_3(x,y)$ or amplitude $s_3(x,y)$ images only (Supplementary Information).[33] Figure 2f shows $|\hat{\sigma}_3(k_x,k_y)|^2 = |\mathcal{F}[\sigma_3(x,y)]|^2$ of the complex-valued s-SNOM images of the 13 nm thick ML-hBN. A bright ring is observed (in contrast to the FT of the topography image in Figure 2c), revealing a well-defined isotropic periodicity of the pattern observed in the near-field images. Importantly, the diameter of the ring increases with ν, thus indicating PhPs that propagate in all directions.

To verify our interpretation and to establish a quantitative analysis of the FT to measure the PhP dispersion, we developed an analytical model. Considering that the thickness of the ML-hBN is much smaller than the polariton wavelength, the sample is described by a conductive sheet layer[34,35] (on a SiO$_2$/Si substrate) with the dielectric function shown by the red curves in Figure 1e, which contains randomly distributed PhP scatterers (illustrated in Figure 1g). The tip is modeled as a point dipole source launching PhPs and we consider only single scattering events at the nearest scatterers. The total complex-valued electric field below the dipole source, mimicking the s-SNOM signal, is calculated as a function of the dipole position, $\sigma(x,y) = s(x,y)e^{i\varphi(x,y)}$ (see Methods). For a PhP scatterer density of 30 μm^{-2} and a layer thickness of 13 nm, the calculated phase images $\varphi(x,y)$ and FT $|\hat{\sigma}(k_x,k_y)|^2 = |\mathcal{F}[\sigma(x,y)]|^2$ match well the experimental results of Figure 2f, supporting our assumption that the IR near-field pattern stems from propagating PhPs scattering at randomly distributed defects. More important, the model allows us to derive an analytical expression for fitting $|\hat{\sigma}(k)|^2$ according to:

7

$$|\hat{\sigma}(k)|^2 \sim \frac{1}{\sqrt{\left(k^2 - 4\left[(k_p')^2 - (k_p'')^2\right]\right)^2 + 64(k_p')^2(k_p'')^2}} \qquad (1)$$

where $k = \sqrt{k_x^2 + k_y^2}$ and the complex-valued polariton momentum $k_p = k_p' + ik_p''$ is the only fitting parameter describing the single mode supported by the layer, i.e. the M0 mode (see Methods and Supplementary Information).

Figure 3a shows, by way of an example, the fitting (blue curve) of a radially averaged FT of the complex-valued s-SNOM image (black curve) of a 19 nm thick ML-hBN at 1420 cm⁻¹. Analogous fitting of the complex-valued s-SNOM images of hBN layers of various thicknesses (one- to four-fold stacked ML-hBNs) yields the PhP dispersions $v(k_p')$ shown in Figure 3b (dots). Comparing the PhP dispersion for the 24 nm ML-hBN (purple dots) with the dispersion obtained from the spacing of the interference fringes (black crosses, described above), we find excellent agreement between the two different measurements, validating the dispersion measurement via fitting the FT of the complex-valued s-SNOM images by Equation 1.

From the fitting to radially averaged FT of the complex-valued s-SNOM images we also obtained the imaginary part of the polariton wavevectors, k_p'', yielding the PhP propagation lengths $L_p = 1/k_p''$ and PhP lifetimes $\tau_{\text{field}} = L_p/v_g$, where $v_g = d\omega/dk_p'$ with ω the angular frequency (dots in Figure 3c and d, respectively). Altogether, the results reveal the typical behavior of PhPs: (i) the wavevector k_p' increases as the wavenumber increases and the thickness decreases (Figure 3b), (ii) the propagation length L_p decreases with increasing wavenumber and decreasing thickness (Figure 3c), and (iii) the lifetime τ_{field} is rather independent of wavenumber and thickness (Figure 3d). Importantly, τ_{field} of about 0.6 ps is only factor of about two smaller than the PhP lifetime in high-quality hBN (indicated by grey solid curve in Figure 3d).

For comparison, we calculated the PhP dispersions, propagation lengths and lifetimes using the dielectric function of hBN obtained in Figure 1e (solid lines in Figure 3b and d; see Methods). A good agreement with experiment and theory is found for all ML-hBN thicknesses, corroborating that the random fringe patterns indeed reveal propagating PhPs that seem to randomly scatter at nanoscale defects. Further, it shows that the dielectric function of the ML-hBN obtained by far-field reflection spectroscopy essentially reveals the optical material properties between the PhP scattering centers where the PhPs propagate. Thus, the PhP scattering centers do not significantly influence the macroscopic dielectric function and we can conclude that the increased phonon damping as compared to ME-hBN flakes rather stems from homogenously distributed atomic scale defects, which might be originating from the polycrystallinity of CVD ML-hBN as confirmed by TEM characterization (Figure 1b). To test the reproducibility of our PhP observations, we recorded s-SNOM images of two further

8

samples (see Figure S6), where the ML-hBN layers were grown in separate but similar CVD processes. In the s-SNOM images of these samples we observed again the random PhP interference patterns, from which we determined the PhP wavevectors. These wavevectors agree well with calculated PhP wavevectors using the dielectric function shown in Figure 1e, thus demonstrating reproducibility of the ML-hBN layer growth and PhP properties (Supplementary Section 7).
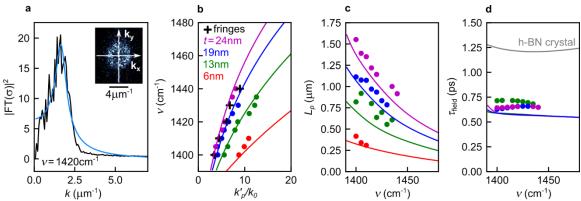

Figure 3. Comparison of measured and calculated PhP properties. (a) Black curve shows radially averaged FT of the complex-valued s-SNOM image of a 19 nm thick ML-hBN at 1420 cm⁻¹. Blue curve shows the fit by Equation 1. Inset shows $|\hat{\sigma}_3(k_x, k_y)|^2$. (b,c) PhPs dispersion and propagation length for stacked ML-hBNs of different total thicknesses t. Dots show results obtained from fitting the FTs of the various complex-valued s-SNOM images, analogue to panel a. Solid lines show calculated PhP dispersions using the dielectric function of the ML-hBN shown in Figure 1e. Black crosses show the PhP dispersion obtained for the 24 nm thick ML-hBN (Figure 2d) by measuring the spacing of the interference fringes parallel to the edge. d) Calculated (colored lines) and measured (dots; obtained from panels b and d as $\tau_{\text{field}} = L_p/v_g$) PhP lifetimes. Grey: calculated PhP lifetime in a 13 nm thick ME-hBN.[28]

We finally explore the possibility to fabricate PhP nanoresonators from the ML-hBN, which could be applied in the future for surface-enhanced infrared absorption spectroscopy (SEIRA)[9] or for gas sensing. [36] In **Figure 4** we show far- and near-field IR spectroscopy studies (illustrated in Figure 4a and f) of ribbons arrays fabricated by e-beam lithography and reactive-ion etching (RIE) of a 13 nm thick ML-hBN obtained by stacking two individual CVD ML-hBN (Methods). Owing to the large-scale homogeneous hBN layers, we could fabricate 30 arrays of 40x40 μm², allowing for systematic variation of the ribbon width w. The far-field reflection spectra (Methods) of the ribbon arrays clearly show peaks that shift to higher wavenumbers as the ribbon width w decreases (Figure 4b), thus indicating PhP

9

resonances.[9,10] Simulations for the far-field reflection spectra (Methods) employing the dielectric function of the ML-hBN (shown in Figure 1e) reproduce well the experimental reflection spectra. We first elucidate the spatial distribution of the resonating PhP mode by s-SNOM imaging of the 156 nm wide ribbons near their resonance peak at 1450 cm^{-1} (Figure 4g). We find a strong near-field amplitude signal s_3 at the ribbon edges and a rather weak signal in the ribbon center, which corresponds to a strong near-field concentration at the ribbon edges. The resonance can be thus attributed to a dipolar mode, which is confirmed by the calculated spatial near-field distribution across one ribbon shown in Figure 4h. We note that the near-field signal variations along the ribbon edges in the s-SNOM image can be attributed to local variations in the ribbon width, polycrystallinity of CVD ML-hBN and fabrication damage.
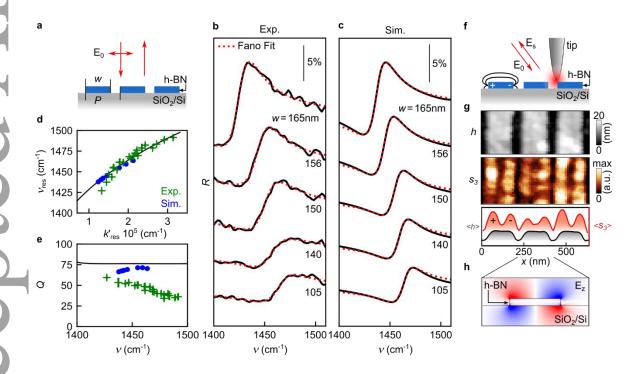

Figure 4. Far- and near-field characterization ribbons fabricated from a 13nm thick ML-hBN. a) Schematics of far-field infrared reflection spectroscopy experiment. b,c) Black curves: measured and simulated reflection spectra of hBN ribbon arrays of different w. Red dashed lines: fits with Fano line shapes. d) Green crosses and blue dots: PhP dispersions obtained from Fano fits of measured and simulated reflection spectra, respectively, and assuming Fabry-Perot resonances transverse to the ribbons (Methods). Black curve: calculated PhP dispersion (Methods) for a 13 nm ML-hBN with the dielectric function shown in Figure 1e. e) Quality factors of the ribbon resonances obtained from the Fano fits of the measured (green crosses) and simulated (blue dots) ribbon resonances. Black curve: calculated Q from calculated lifetime in Figure 3d. f) Schematics of the near-field imaging experiment. g) Topography (showing height h, top) and near-field amplitude (s_3, center) images of $w = 156$ nm wide hBN ribbons near the resonance wavenumber ν (1450 cm^{-1}). Bottom graph shows averaged topography

10

and near-field amplitude line profiles across the ribbons. h) Simulated cross section of the electric near-field distribution (vertical field component E_z) of a single hBN ribbon with $w = 156$ nm.

To quantify and interpret the dipolar modes, we extracted for each ribbon array the resonance wavenumber ν_{res} and linewidth $\Delta\nu$. To that end, we fitted a Fano lineshape (red dotted curves in Figure 4b and c) to the measured and simulated spectra (black curves in Figure 4b and c) to account for the peak asymmetry, due to the interference between light scattered at the ribbons and reflected at the SiO_2/Si surface (see Methods). An excellent fitting is achieved. From the dipolar near-field distribution observed in Figure 4g, we assume that the peaks correspond to the first-order longitudinal Fabry-Perot PhP resonance of the fundamental PhP mode (typically referred as the M0 mode). We can attribute then a PhP wavevector $k_{res} = (\pi - \theta)/w$ to each resonance, where $\theta = 0.32\pi$ is the PhP reflection phase at the ribbon edges (see Supplementary Information) and w is the ribbon width, which was measured by scanning electron microscopy. In Figure 4d we show $\nu_{res}(k_{res})$ obtained from the measured (green crosses) and simulated spectra (blue dots). They agree well with each other and the positions of the spectral maxima match the calculated PhP dispersion (black solid line) for an unstructured ML-hBN with the dielectric function shown in Figure 1e, confirming that the resonances are caused by PhP modes propagating forth and back transversely to the hBN ribbons. From the materials science perspective, the remarkable match between the calculated and the measured PhP dispersions in Figure 4d demonstrates that the CVD growth process yields hBN layers of homogeneous thickness and dielectric function on the millimeter-scale, since the individual ribbon arrays are distributed over an area of about 0.5x0.5 mm^2.

From the linewidths $\Delta\nu$ we determined the quality factor of the resonances according to $Q = \omega_{res}/\Delta\omega = \nu_{res}/\Delta\nu$. The experimental Q (green crosses in Figure 4e) decreases from about 60 to 30 with decreasing ribbon width w, while the estimated Q from the simulated spectra is about 70 (blue dots in Figure 4e). We explain the reduced experimental Q by additional PhP damping due to fabrication-induced damage and roughness at the ribbon edges, similar to what has been reported for PhP resonances in ribbons made of ME-hBN.[9] We also show in Figure 4e the theoretical limit, $Q_{lim} = \omega\tau = 2\pi c\nu\tau$ (black line), where $\tau = 1/\Delta\omega$ is the theoretical limit of the PhP lifetime according to $\tau = \tau_{field}/2$ with $\tau_{field} = L_p/v_g$ (blue curve in Figure 3d). Note that τ in standard far-field spectroscopy defines the time in which the intensity of an excitation decays to $1/e$ of its initial value, implying that $\tau = \tau_{field}/2$.[37] We obtain a Q_{lim} of about 77, slightly larger than the estimated Q from the simulated ribbon spectra, revealing that the damping of the simulated PhP resonances is dominated by PhP dissipation (governed by the imaginary part of the dielectric function of ML-hBN) rather than by radiation losses. We note the rather large quality factors seem to contradict the short relative PhP propagation lengths, that is, the observation of only a few polariton fringes near the hBN edges in the s-SNOM images shown in Figure 2. To clarify this issue, we express the relative polariton propagation length, L_p/λ_p, as a function of the quality factor Q[33]:

11

$$\frac{L_p}{\lambda_p} = \frac{k_p'}{2\pi k_p''} = \frac{1}{\pi}\frac{v_g}{c}qQ, \qquad\qquad (2)$$

where $q = k_p'/k_0$ with k_0 being the wavevector of the photon. We find that L_p/λ_p does not only scale with Q but also with the group velocity v_g, which for PhP in thin layers is typically two or three orders of magnitude smaller than c [38]. For that reason, we obtain $L_p/\lambda_p = 1$ for PhPs at 1435 cm^{-1} and and hBN layer thickness of 13 nm, where $q = 12.6$ and $v_g = 3.24 \ 10^{-3} \ c$. This quite short relative propagation length is fully consistent with the few PhP fringes observed in Figure 2f.

3. Conclusion

In summary, we employed IR nanoimaging to demonstrate that millimeter-size ML-hBN of 6 nm thickness can support, individually or when stacked, PhPs with lifetimes up to 0.6 ps, being only a factor of two reduced compared to that of phonon polaritons in high-quality ME-hBN flakes. On the other hand, IR nanoimaging showed random PhP interference patterns, which could be explained by the presence of defects acting as strong PhP scatterers that are not recognized by other techniques such as far-field infrared spectroscopy, Raman spectroscopy or scanning and transmission electron microscopy. Thus, the analysis of PhP interference patterns may become a valuable method for quality assessment of CVD-grown 2D materials and for studying growth defects. Artificial intelligence may be applied to analyze the s-SNOM images[39–41], based on a training of a neural network with simulated polariton interference patterns (according to the model presented in this work) obtained for different defect distributions. Intriguingly, despite strong PhP scattering, ML-hBN already allowed for the fabrication of Fabry-Perot phonon polariton resonators with remarkable quality factors up to $Q \approx 50$, clearly demonstrating the potential of ML-hBN for large-scale fabrication of PhP nanoresonator devices for infrared gas sensing[36] and phonon-polariton-assisted detection of infrared radiation.[42]

4. Methods

CVD growth of hBN layers

ML-hBN was grown on c-plane Al$_2$O$_3$ (0001) at 1400°C, 500 mbar for 30 mins in an AIXTRON CCS 2D reactor. Borazine was used as a precursor, with 10 sccm N$_2$ to transport it. Prior to hBN growth, the substrate was annealed in H$_2$ for 10 mins at 150 mbar and 1200°C. ML-hBN was then wet transferred on SiO$_2$/Si$^+$ (285 nm/500 μm) substrates and TEM grids as described in the following.

Transfer of ML-hBN

ML-hBN was spin-coated with poly(methyl methacrylate) (PMMA) A4 950 at 1000 rpm for 1 min and baked at 80 °C for 10 mins. The PMMA coated ML-hBN on sapphire was kept in 8% H$_3$PO$_4$ for about 10 h to delaminate it. The delaminated PMMA/hBN was kept in deionized (DI) water for 1-2 h. For the transfer on SiO$_2$/Si, the cleaned PMMA/hBN in DI water was scooped out with SiO$_2$/Si and left drying for > 5 h. The PMMA/hBN on SiO$_2$/Si was baked at 80 °C for 10 mins and soaked in acetone and

12

isopropyl alcohol (IPA) to remove the PMMA. To transfer another ML-hBN on a transferred ML-hBN on SiO₂/Si, the same procedure was followed, but PMMA/ML-hBN was scooped out with hBN/SiO₂/Si. To transfer ML-hBN on TEM grids, these were fixed on a glass slide with a tape and the already delaminated and cleaned PMMA/ML-hBN in DI water was scooped out with the TEM grid on glass and left drying for > 5 h. The PMMA/ML-hBN on TEM grid/glass was baked at 80 ºC for 10 mins and soaked in acetone and IPA to remove the PMMA.

Raman spectroscopy of hBN layers

As grown and transferred ML-hBN was characterized by Raman spectroscopy with a Renishaw InVia instrument equipped with a 100x objective and illumination at 514.5 nm wavelength. A statistical analysis of 8 spectra on as grown ML-hBN on sapphire, 6 on ML-hBN on TEM grids, 12 on about 6-nm thick ML-hBN on SiO₂/Si and 10 spectra on about 13 nm-thick ML-hBN on SiO₂/Si was performed to find the frequency $\omega_{E_{2g}}$ and linewidth $\gamma_{E_{2g}}$ of the ML-hBN E_{2g} peak.[26] The errors were calculated from the standard deviation across different spectra and the spectrometer resolution of about 1 cm⁻¹. We find ω_{E2g} of 1371 ± 1 cm⁻¹ for the as-grown ML-hBN on sapphire and 1368 ± 1 cm⁻¹ for the 1 nm thick ML-hBN transferred on TEM grid, 6 nm thick ML-hBN and 13 nm thick ML-hBN transferred on SiO2 substrate. While the linewidths γ_{E2g} are respectively 20 ± 2 cm⁻¹, 19 ± 1 cm⁻¹, 21 ± 2 cm⁻¹, 20 ± 2 cm⁻¹.

Far-field FTIR reflection spectroscopy of hBN layers and ribbons

Reflection spectra of the ML-hBN (example shown in inset of Figure 1e) were recorded with a Bruker Hyperion 2000 infrared microscope (Bruker Optics GmbH, Ettlingen, Germany) equipped with a 15x Cassegrain objective and coupled to a Bruker Vertex 70 FTIR spectrometer (Bruker Optics GmbH, Ettlingen, Germany). The spectra of the sample were normalized to the reflection spectrum of a gold mirror. The spectra of the ribbon arrays were measured with linear polarization (using a wire grid polarizer) perpendicular to the ribbons and normalized to the reflection spectrum of the clean Si/SiO₂ substrate. The spectral resolution was set to 2 cm⁻¹.

Dielectric functions of ML-hBN, SiO₂ and Si from far-field FTIR reflection spectra

We used a multilayer model based on the complex-valued Fresnel formulas[43] to fit the reflection spectra of the bare SiO₂/Si substrate and the ML-hBN/SiO₂/Si sample. Specular reflection with an incident angle of 17° was considered. The dielectric functions were used as fit parameters. First, we determined the dielectric function of SiO₂ and Si from the reflection spectra of the bare SiO₂/Si substrate, which was described as a 285 nm thick SiO₂ layer on a semi-infinite Si bulk material. The dielectric function of SiO₂ was modeled with two Lorentz oscillators and the free carriers in the Si substrate was described via the Drude model according to the following equations:

$$\varepsilon_{\text{SiO2}}(v) = \varepsilon_{\text{SiO2},\infty} + \sum_{k=1,2} \frac{S_k v_k^2}{v_k^2 - v^2 - i v \Gamma_k} \tag{2}$$

$$\varepsilon_{\text{Si}}(v) = \varepsilon_{\text{Si},\infty} - \frac{v_p^2}{v^2 - i v \Gamma_p} \tag{3}$$

13

where $\varepsilon_{k,\infty}$ are the high-frequency permittivity of Si and SiO$_2$, and the parameters S_k, ν_i and Γ_k are the oscillator strengths, frequencies and dampings, respectively. We obtained from the fit the following values: $\varepsilon_{\text{Si},\infty}= 12$, $\varepsilon_{\text{SiO2},\infty}= 2.34$, $S_1 = 0.1$, $S_2 = 0.8$, $\nu_1 = 806$ cm^{-1}, $\nu_2 = 1078$ cm^{-1}, $\Gamma_1 = 63$ cm^{-1}, and $\Gamma_2 = 31$ cm^{-1}. For the screened plasma frequency and damping we obtained $\nu_p = 2400$ cm^{-1} and $\Gamma_p = 410$ cm^{-1}, respectively.

The dielectric function of ML-hBN was obtained by fitting the reflection spectra of the ML-hBN layer on SiO$_2$/Si. The sample was described as a 6 nm thick ML-hBN (thickness measured by AFM, Figure 1b) on a 285 nm thick SiO$_2$ layer on a semi-infinite bulk Si, which were described with the dielectric functions provided above. The in-plane dielectric function of the ML-hBN were described by a Lorenz oscillator according to

$$\varepsilon_\perp(\nu) = \varepsilon_{\perp,\infty} + \varepsilon_{\perp,\infty} \frac{\nu_{\perp,\text{LO}}^2 - \nu_{\perp,\text{TO}}^2}{\nu_{\perp,\text{TO}}^2 - \nu^2 - i\nu\Gamma_\perp} \tag{4}$$

While the out-of-plane parameters was fixed to the constant value of $\varepsilon_{\parallel,\infty}= 2.95$ (as reported in [28]), since it is irrelevant for the investigated frequency range. From the fitting of the reflection spectrum we obtained in-plane high-frequency permittivity, $\varepsilon_{\perp,\infty}= 4.7$, transverse optical phonon frequency, $\nu_{\perp,\text{TO}}= 1369$ cm^{-1}, longitudinal phonon frequency, $\nu_{\perp,\text{LO}} = 1621$ cm^{-1} and damping, $\Gamma_\perp = 19$ cm^{-1}.

Scattering-type scanning near-field optical microscopy (s-SNOM)

We used a commercial s-SNOM setup (neaSNOM, Attocube AG). A Pt/Ir coated atomic force microscope tip, with a curvature radius $a \approx 25 \, nm$, (Arrow-NCPt-50, NanoWorld AG) was illuminated by p-polarized infrared radiation generated by a tunable quantum cascade lasers (QCL, Daylight Solutions) with an average power of about 3 mW. The tip-scattered field was detected with a pseudo-heterodyne interferometric module. To suppress background scattering, the tip was oscillating at a frequency $\Omega \cong 270$ KHz and the interferometric detector signal was demodulated at a frequency 3Ω, yielding near-field amplitude and the phase signals, s_3 and φ_3, respectively.

Simulation of s-SNOM images of Figure 3h

We have developed an analytical model to simulate near-field images (Figure 2g and h) and to analyze their FTs (Figure 3a). We model the s-SNOM tip as a point dipole, which (i) excites PhPs that propagate along the ML-hBN with wavevector k_p and (ii) scatters (into free-space radiation) the PhPs that are backscattered by the defects in the ML-hBN. Each defect (numerated by j) is modelled as a point scatter with a polarizability α_j. We applied first order perturbation theory by considering that the defects interact only with the PhPs launched by the tip, but not with PhPs that are scattered at the defects. The z-component of the total PhP field scattered by the tip at position r = (x,y) is obtained according to

14

$$\Delta E_z(\boldsymbol{r}) \sim \sum_j \alpha_j \frac{e^{2ik_p|r-r_j|}}{|r-r_j|}, \tag{5}$$

where $\boldsymbol{r}_j$ is the positions of the *j-th* defect. The summation is carried out over all defects. FT of Equation 5 yields Equation 1 of the main text. In Supplementary Information we discuss the analytical model in more detail. Note that in the s-SNOM experiments there is an additional tip-scattered field, which originates from the tip-sample near-field interaction induced by the incident field, $E_{z,0}(\boldsymbol{r})$.[44] Considering, in first approximation, that spatial variations of this near-field interaction are negligible compared to the spatial signal variations caused by PhP scattering, we set $E_{z,0}(\boldsymbol{r}) = E_{z,0} = const$. We subsequently obtained the simulated images shown in Figure 2h of the main text according to

$$\sigma(x,y) = s(x,y)e^{i\varphi(x,y)} = E_{z,0} + \Delta E_z(x,y) \tag{6}$$

where we set $E_{z,0}$ to a value larger than the maximum value of $|\Delta E_z(x,y)|$.

Fourier transform of measured and simulated complex-valued s-SNOM images

We calculated the squared modulus of 2D Fourier transform of the complex-valued signal $\sigma(x,y) = s(x,y)e^{i\varphi(x,y)}$, where $s(x,y)$ and $\varphi(x,y)$ are the s-SNOM amplitude and phase images, according to

$$|\hat{\sigma}(k_x,k_y)|^2 = \left|\iint dx\, dy\, H(x,y)\sigma(x,y)\, e^{-2\pi i(k_x x + k_y y)}\right|^2. \tag{7}$$

Where $H(x,y)$ is the Hann window function,[45] used to reduce artifacts due to the finite size of the images. Radial profiles of $\hat{\sigma}$ were obtained by calculating the angular average of $|\hat{\sigma}(k_x,k_y)|^2$ at a given distance $k = \sqrt{k_x^2 + k_y^2}$ from the origin.

Calculation of PhP dispersion, propagation length and lifetime

To calculate the PhP dispersion $v(k_p')$, propagation length $L_p = 1/k_p''$, and lifetime $\tau_{\text{field}} = L_p/v_g$ with group velocity $v_g = d\omega/dk_p'$, we determined the complex-valued wavevector $k_p = k_p' + ik_p''$ form the calculated complex-valued Fresnel reflection coefficient r_p of the ML-hBN/SiO₂/Si samples by employing the multilayer transfer matrix approach.[46] To that end, we determined the poles of $r_p(k_p' + ik_p'', v)$ by solving numerically the equation $1/\text{Abs}(r_p) = 0$. For ML-hBN, SiO₂ and Si we used the dielectric functions obtained by fitting the far-field reflection spectra as described above.

Fabrication of ML-hBN ribbons

Arrays of ML-hBN ribbons (Figure 4) were fabricated by high-resolution electron beam lithography (EBL, Raith 150TWO). First, PMMA was spin-coated onto the ML-hBN on the SiO₂/Si substrates.

15

Second, a 2 nm thick Au layer was sputtered onto the e-beam resist as a conductive layer to avoid charging. Ribbon arrays with a size of 60 x 60 μm^2 were patterned by EBL within homogenous areas of the ML-hBNs, which were identified by optical inspection with a light microscope. The conductive layer was removed after e-beam exposure by immersing the sample in Au etchant for 10 s, followed by rinsing in water and IPA. The sample was then developed in MIBK(methyl isobutyl ketone):IPA (3:1) and rinsed in IPA. In the following, a hard mask to protect the ML-hBN during the etching process was fabricated by e-beam evaporation of 3 nm of Cr and thermal evaporation of 50 nm Al layer in ultrahigh vacuum. Lift-off in acetone yields a structured hard metal mask on the ML-hBN. The uncovered ML-hBN areas were reactive ion etched (RIE Oxford Plasmalab 80 Plus) using a 20 sccm SF_6/Ar 1:1 flow and a 100 W plasma power at 100 mTorr pressure for 40 s. The Cr/Al hard mask was chemically etched using a Cr etchant solution and rinsed in DI water. Finally, the sample was cleaned by rinsing it in IPA and drying with a N_2 gun.

Fitting of the far-field FTIR reflection spectra of hBN ribbons

The reflection spectra of the ML-hBN ribbons arrays (Figure 4b and c) exhibit an asymmetric lineshape, which results from the interference between the radiation reflected at the SiO_2/Si substrate and that scattered by the hBN ribbons. To extract the spectral resonance positions, ν_{res}, and the linewidths, $\Delta\nu$, of the PhP resonances, we performed a Fano fit to the measured and simulated reflection spectra according to[47]

$$R(\nu) \propto \frac{(\epsilon+q)^2}{(1+\epsilon^2)} \tag{8}$$

where q is the Fano parameter and $\epsilon = 2\frac{\nu-\nu_{res}}{\Delta\nu}$.

Simulation of ML-hBN ribbon arrays reflection spectra

The simulated reflection spectra of ribbon arrays on the SiO_2/Si substrate (Figure 4c) were obtained by full-wave numerical simulations using the finite-elements method in frequency domain (COMSOL Multiphysics). We used the dielectric functions obtained from fitting the far-field reflection spectra of hBN, SiO_2 and Si. We assumed a semi-infinite Si substrate with 285 nm SiO_2 on top. The ML-hBN thickness and ribbon width are provided in Figure 4c.

16

Competing interests

R.H. is co-founder of Neaspec GmbH, a company producing scattering-type scanning near-field optical microscope systems, such as the one used in this study. The remaining authors declare no competing interests.

Supporting Information

Supporting Information is available from the Wiley Online Library or from the author.

Data availability statement

The data that support the findings of this study are available from the corresponding author upon reasonable request.

References

[1] D. N. Basov, M. M. Fogler, F. J. García de Abajo, *Science* **2016**, *354*, aag1992.

[2] T. Low, A. Chaves, J. D. Caldwell, A. Kumar, N. X. Fang, P. Avouris, T. F. Heinz, F. Guinea, L. Martin-Moreno, F. Koppens, *Nat. Mater.* **2017**, *16*, 182.

[3] G. X. Ni, A. S. McLeod, Z. Sun, L. Wang, L. Xiong, K. W. Post, S. S. Sunku, B.-Y. Jiang, J. Hone, C. R. Dean, M. M. Fogler, D. N. Basov, *Nature* **2018**, *557*, 530.

[4] S. Dai, Z. Fei, Q. Ma, A. S. Rodin, M. Wagner, A. S. McLeod, M. K. Liu, W. Gannett, W. Regan, K. Watanabe, T. Taniguchi, M. Thiemens, G. Dominguez, A. H. C. Neto, A. Zettl, F. Keilmann, P. Jarillo-Herrero, M. M. Fogler, D. N. Basov, *Science* **2014**, *343*, 1125.

[5] W. Ma, P. Alonso-González, S. Li, A. Y. Nikitin, J. Yuan, J. Martín-Sánchez, J. Taboada-Gutiérrez, I. Amenabar, P. Li, S. Vélez, C. Tollan, Z. Dai, Y. Zhang, S. Sriram, K. Kalantar-Zadeh, S.-T. Lee, R. Hillenbrand, Q. Bao, *Nature* **2018**, *562*, 557.

[6] J. Taboada-Gutiérrez, G. Álvarez-Pérez, J. Duan, W. Ma, K. Crowley, I. Prieto, A. Bylinkin, M. Autore, H. Volkova, K. Kimura, T. Kimura, M.-H. Berger, S. Li, Q. Bao, X. P. A. Gao, I. Errea, A. Y. Nikitin, R. Hillenbrand, J. Martín-Sánchez, P. Alonso-González, *Nat. Mater.* **2020**, *19*, 964.

[7] Q. Zhang, G. Hu, W. Ma, P. Li, A. Krasnok, R. Hillenbrand, A. Alù, C.-W. Qiu, *Nature* **2021**, *597*, 187.

[8] D. Rodrigo, O. Limaj, D. Janner, D. Etezadi, F. J. García de Abajo, V. Pruneri, H. Altug, *Science* **2015**, *349*, 165.

[9] M. Autore, P. Li, I. Dolado, F. J. Alfaro-Mozaz, R. Esteban, A. Atxabal, F. Casanova, L. E. Hueso, P. Alonso-González, J. Aizpurua, A. Y. Nikitin, S. Vélez, R. Hillenbrand, *Light Sci. Appl.* **2018**, *7*, 17172.

17

[10] M. Autore, I. Dolado, P. Li, R. Esteban, F. J. Alfaro-Mozaz, A. Atxabal, S. Liu, J. H. Edgar, S. Vélez, F. Casanova, L. E. Hueso, J. Aizpurua, R. Hillenbrand, *Adv. Opt. Mater.* **2021**, *9*, 2001958.

[11] F. J. Alfaro-Mozaz, P. Alonso-González, S. Vélez, I. Dolado, M. Autore, S. Mastel, F. Casanova, L. E. Hueso, P. Li, A. Y. Nikitin, R. Hillenbrand, *Nat. Commun.* **2017**, *8*, 15624.

[12] I. Dolado, F. J. Alfaro-Mozaz, P. Li, E. Nikulina, A. Bylinkin, S. Liu, J. H. Edgar, F. Casanova, L. E. Hueso, P. Alonso-González, S. Vélez, A. Y. Nikitin, R. Hillenbrand, *Adv. Mater.* **2020**, *32*, 1906530.

[13] P. Pons-Valencia, F. J. Alfaro-Mozaz, M. M. Wiecha, V. Biolek, I. Dolado, S. Vélez, P. Li, P. Alonso-González, F. Casanova, L. E. Hueso, L. Martín-Moreno, R. Hillenbrand, A. Y. Nikitin, *Nat. Commun.* **2019**, *10*, 3242.

[14] E. J. C. Dias, R. Yu, F. J. García de Abajo, *Light Sci. Appl.* **2020**, *9*, 87.

[15] Y. Wu, J. Ordonez-Miranda, S. Gluchko, R. Anufriev, D. D. S. Meneses, L. Del Campo, S. Volz, M. Nomura, *Sci. Adv.* **2020**, *6*, eabb4461.

[16] X. Li, W. Cai, J. An, S. Kim, J. Nah, D. Yang, R. Piner, A. Velamakanni, I. Jung, E. Tutuc, S. K. Banerjee, L. Colombo, R. S. Ruoff, *Science* **2009**, *324*, 1312.

[17] N. Jr. Bareza, K. K. Gopalan, R. Alani, B. Paulillo, V. Pruneri, *ACS Photonics* **2020**, *7*, 879.

[18] H. Hu, X. Yang, X. Guo, K. Khaliji, S. R. Biswas, F. J. García de Abajo, T. Low, Z. Sun, Q. Dai, *Nat. Commun.* **2019**, *10*, 1131.

[19] F. H. L. Koppens, T. Mueller, Ph. Avouris, A. C. Ferrari, M. S. Vitiello, M. Polini, *Nat. Nanotechnol.* **2014**, *9*, 780.

[20] S.-J. Yu, Y. Jiang, J. A. Roberts, M. A. Huber, H. Yao, X. Shi, H. A. Bechtel, S. N. Gilbert Corder, T. F. Heinz, X. Zheng, J. A. Fan, *ACS Nano* **2022**, *16*, 3027.

[21] A. Mancini, L. Nan, F. J. Wendisch, R. Berté, H. Ren, E. Cortés, S. A. Maier, *ACS Photonics* **2022**, *9*, 3696.

[22] C. Ashworth, *Nat. Rev. Phys.* **2020**, *2*, 176.

[23] T.-A. Chen, C.-P. Chuu, C.-C. Tseng, C.-K. Wen, H.-S. P. Wong, S. Pan, R. Li, T.-A. Chao, W.-C. Chueh, Y. Zhang, Q. Fu, B. I. Yakobson, W.-H. Chang, L.-J. Li, *Nature* **2020**, *579*, 219.

[24] K. Y. Ma, L. Zhang, S. Jin, Y. Wang, S. I. Yoon, H. Hwang, J. Oh, D. S. Jeong, M. Wang, S. Chatterjee, G. Kim, A.-R. Jang, J. Yang, S. Ryu, H. Y. Jeong, R. S. Ruoff, M. Chhowalla, F. Ding, H. S. Shin, *Nature* **2022**, *606*, 88.

[25] S. Dai, W. Fang, N. Rivera, Y. Stehle, B. Jiang, J. Shen, R. Y. Tay, C. J. Ciccarino, Q. Ma, D. Rodan-Legrain, P. Jarillo-Herrero, E. H. T. Teo, M. M. Fogler, P. Narang, J. Kong, D. N. Basov, *Adv. Mater.* **2019**, *31*, 1806603.

18

[26] S. Reich, A. C. Ferrari, R. Arenal, A. Loiseau, I. Bello, J. Robertson, *Phys. Rev. B* **2005**, *71*, 205201.

[27] R. V. Gorbachev, I. Riaz, R. R. Nair, R. Jalil, L. Britnell, B. D. Belle, E. W. Hill, K. S. Novoselov, K. Watanabe, T. Taniguchi, A. K. Geim, P. Blake, *Small* **2011**, *7*, 465.

[28] A. J. Giles, S. Dai, I. Vurgaftman, T. Hoffman, S. Liu, L. Lindsay, C. T. Ellis, N. Assefa, I. Chatzakis, T. L. Reinecke, J. G. Tischler, M. M. Fogler, J. H. Edgar, D. N. Basov, J. D. Caldwell, *Nat. Mater.* **2018**, *17*, 134.

[29] E. Y. Ma, J. Hu, L. Waldecker, K. Watanabe, T. Taniguchi, F. Liu, T. F. Heinz, *Nano Lett.* **2022**, *22*, 8389.

[30] N. Ocelic, A. Huber, R. Hillenbrand, *Appl. Phys. Lett.* **2006**, *89*, 101124.

[31] Z. Zheng, J. Chen, Y. Wang, X. Wang, X. Chen, P. Liu, J. Xu, W. Xie, H. Chen, S. Deng, N. Xu, *Adv. Mater.* **2018**, *30*, 1705318.

[32] A. Bylinkin, M. Schnell, M. Autore, F. Calavalle, P. Li, J. Taboada-Gutièrrez, S. Liu, J. H. Edgar, F. Casanova, L. E. Hueso, P. Alonso-Gonzalez, A. Y. Nikitin, R. Hillenbrand, *Nat. Photonics* **2021**, *15*, 197.

[33] S. Chen, A. Bylinkin, Z. Wang, M. Schnell, G. Chandan, P. Li, A. Y. Nikitin, S. Law, R. Hillenbrand, *Nat. Commun.* **2022**, *13*, 1374.

[34] J. S. Gomez-Diaz, M. Tymchenko, A. Alù, *Phys. Rev. Lett.* **2015**, *114*, 233901.

[35] A. Y. NIKITIN, in *World Sci. Handb. Metamaterials Plasmon. Vol. 4 Recent Prog. Field Nanoplasmonics*, World Scientific, **2018**, pp. 307–338.

[36] N. Jr. Bareza, B. Paulillo, T. M. Slipchenko, M. Autore, I. Dolado, S. Liu, J. H. Edgar, S. Vélez, L. Martín-Moreno, R. Hillenbrand, V. Pruneri, *ACS Photonics* **2022**, *9*, 34.

[37] L. Novotny, B. Hecht, *Principles of Nano-Optics*, Cambridge University Press, Cambridge, **2012**.

[38] E. Yoxall, M. Schnell, A. Y. Nikitin, O. Txoperena, A. Woessner, M. B. Lundeberg, F. Casanova, L. E. Hueso, F. H. L. Koppens, R. Hillenbrand, *Nat. Photonics* **2015**, *9*, 674.

[39] X. Chen, Z. Yao, S. Xu, A. S. McLeod, S. N. Gilbert Corder, Y. Zhao, M. Tsuneto, H. A. Bechtel, M. C. Martin, G. L. Carr, M. M. Fogler, S. G. Stanciu, D. N. Basov, M. Liu, *ACS Photonics* **2021**, *8*, 2987.

[40] X. Chen, S. Xu, S. Shabani, Y. Zhao, M. Fu, A. J. Millis, M. M. Fogler, A. N. Pasupathy, M. Liu, D. N. Basov, *Adv. Mater.* **2022**, 2109171.

[41] S. Xu, Alexander. S. McLeod, X. Chen, D. J. Rizzo, B. S. Jessen, Z. Yao, Z. Wang, Z. Sun, S. Shabani, A. N. Pasupathy, A. J. Millis, C. R. Dean, J. C. Hone, M. Liu, D. N. Basov, *ACS Nano* **2021**, DOI 10.1021/acsnano.1c07011.

19

[42] S. Castilla, I. Vangelidis, V.-V. Pusapati, J. Goldstein, M. Autore, T. Slipchenko, K. Rajendran, S. Kim, K. Watanabe, T. Taniguchi, L. Martín-Moreno, D. Englund, K.-J. Tielrooij, R. Hillenbrand, E. Lidorikis, F. H. L. Koppens, *Nat. Commun.* **2020**, *11*, 4872.

[43] M. Dressel, G. Grüner, *Electrodynamics of Solids: Optical Properties of Electrons in Matter*, Cambridge University Press, Cambridge, **2002**.

[44] E. Yoxall, M. Schnell, S. Mastel, R. Hillenbrand, *Opt. Express* **2015**, *23*, 13358.

[45] F. J. Harris, *Proc. IEEE* **1978**, *66*, 51.

[46] N. C. Passler, A. Paarmann, *J. Opt. Soc. Am. B* **2017**, *34*, 2128.

[47] V. Giannini, Y. Francescato, H. Amrania, C. C. Phillips, S. A. Maier, *Nano Lett.* **2011**, *11*, 2835.

Infrared nano-imaging reveals propagating phonon polaritons on wafer-scale nanometer thick hexagonal boron nitride grown by chemical vapour deposition.

The material quality allows for the fabrication of phonon polariton nanoresonators with quality factors comparable to those fabricated from the exfoliated material, paving the way for future large-scale applications.

Eugenio Calandrini, Kirill Voronin, Osman Balci, Sachin M. Shinde, Subash Sharma, Maria Barra Burillo, Andrei Bylinkin, Felix Casanova, Luis E. Hueso, Andrei Chuvilin, Clifford McAleese, Ben R. Conran, Xiaochen Wang, Kenneth Teo, Valentyn S. Volkov, Andrea C. Ferrari, Alexey Y. Nikitin, and Rainer Hillenbrand*

Near- and Far-Field Observation of Phonon Polaritons in Wafer Scale Multilayer Hexagonal Boron Nitride Prepared by Chemical Vapor Deposition

ToC figure

20